

Contents lists available at ScienceDirect

International Journal of Mechanical Sciences

journal homepage: www.elsevier.com/locate/ijmecsci





Modal sensitivity analysis of acoustic metamaterials for structural damage detection

Y.F. Xu a,*, G.L. Huang b

- ^a Department of Mechanical and Materials Engineering, University of Cincinnati, Cincinnati, OH 45221, USA
- ^b Department of Mechanical and Aerospace Engineering, University of Missouri, Columbia, MO 65211, USA

ARTICLE INFO

Keywords: Modal sensitivity Acoustic metamaterials Structural dynamics Structural damage Modal analysis

ABSTRACT

Metamaterials have garnered significant research interest over the past few decades, primarily due to their unique properties not found in naturally occurring materials. However, when integrated into operational engineering structures, metamaterials can sustain damage, compromising their extraordinary attributes and potentially leading to structural failure. This work marks a novel advancement in the field of metamaterials research, providing an in-depth analysis into the impact of damage on the structural dynamic properties of finite acoustic metamaterials (AMMs) consisting of periodic locally resonant mass-in-mass units. A modal sensitivity analysis is formulated based on equations of motion of a damaged AMM, along side with associated eigenvalue problem and frequency response functions. The critical role of the internal spring is analytically revealed in determining the effective mass of a damaged unit. To evaluate the effects of damage on AMMs, an extensive numerical investigation is conducted on a finite AMM; an damage index is proposed for measuring the modal deformation of each spring. It is unequivocally demonstrated that frequency response functions, eigenvalues, and mode shapes of damaged AMMs undergo substantial changes at frequencies near bandgaps and these changes diminish as frequencies move away from the bandgaps. This behavior directly corresponds to the frequency-dependent changes in the effective mass of a mass-in-mass unit due to damage. Hence, this work constitutes a leap forward in our understanding of the structural dynamics of damaged metamaterials and offers valuable insights that could facilitate the development of more effective damage identification techniques and the realization of resilient metamaterial-based structures.

1. Introduction

Acoustic metamaterials (AMMs) are engineered structures designed to exhibit effective material properties not found in naturally existing materials [1-5]. Similar to phononic crystals [6,7], AMMs typically consist of small-sized unit cells arranged in a periodic pattern, resulting in frequency ranges within which acoustic/elastic waves are blocked from propagating. These frequency ranges are commonly referred to as bandgaps. AMMs offer potential for various applications for manipulating sound waves and suppressing vibrations [8-11]. In recent years, there has been growing interest in developing locally resonant AMMs, which are designed with explicit resonant mechanisms [12-15]. Locally resonant AMMs are particularly interesting due to their ability to generate bandgaps for waves with wavelengths much larger than the characteristic size of the corresponding carrier structures, enabling low-frequency vibration and sound attenuation. A locally resonant AMM typically includes resonator mechanisms, as first demonstrated in Ref. [1], where hard metal spheres embedded in soft rubber created

such a mechanism, and in-depth analytical modeling and discussion of the mechanism can be found in Refs. [16–19]. Since then, novel designs of locally resonant AMMs have rapidly evolved, including two-dimensional phononic stubbed plates [20], internally resonating lattices [21], metamaterial plates [22], and periodic architected lattices [23]. These innovative designs continue to expand the potential applications and versatility of locally resonant AMMs in various fields.

Although AMMs have shown remarkable properties that can lead to various potential applications, current research often assumes that AMMs are free from damage through manufacturing, installation, and operation. In reality, damage occurrences cannot be ignored, as they significantly shorten the service life of the structure, increase safety risks, and incur maintenance costs [24–26]. For instance, the emergence of additive manufacturing has expanded the capability for realizing various AMM designs [27–29]. However, microscopic and mesoscale defects [30,31], such as porosity, can occur in additively manufactured AMMs and are undesirable, as they contribute to the failure of the

E-mail addresses: xu2yf@uc.edu (Y.F. Xu), huangg@missouri.edu (G.L. Huang).

^{*} Corresponding author.

materials. Additionally, wear and cracks during operation could arise due to factors like workpiece falls, operator inexperience [32], and fatigue [33,34]. Hence, it is essential to develop methods for detecting damage in AMMs at an early stage to guarantee timely maintenance and repairs. Research on AMMs and their potential applications has been ongoing for decades, and there is still much to learn about these materials. By integrating the awareness of damage occurrence into the development of AMMs, the design and manufacturing of more resilient and reliable metamaterial-based structures can be achieved.

Meanwhile, extensive research has been conducted on damage detection for engineering structures and components, investigating both transient and steady-state structural dynamic features. Transient features include acoustic emission (AE) [35,36] and guided waves [37, 38]. AE is an instantaneous result of damage occurrence, referring to the release of sound waves [35,39]. These sound waves typically carry high-frequency energy, and abrupt increases in sound pressure levels can indicate damage in various forms, such as fatigue [40] and cracks [41]. Guided wave damage detection is a well-developed nondestructive evaluation technique based on irregularities in wave propagation due to damage [42-44]. These methods have proved sensitive to small and internal damage, such as delamination [45,46] and debonding [47,48]. However, AE methods often require real-time monitoring, and guided wave methods may need fine-tuned excitation, which in return limit their feasibility. Steady-state features, such as modal strains [49,50] and modal parameters [51], offer more robust damage detection. Strain sensors can detect changes in modal strains, which are effective for localizing damage. One type of such sensor is fiber optic sensor, and they have been applied for structural health monitoring for large-scale infrastructures [52,53]. Vibrationbased methods involve changes in frequency response functions and modal parameters of structures [51,54]. Natural frequencies are considered global properties, while mode shapes and their changes are local properties. Both have proven effective for damage location, but each has its limitations. Recent developments in computer vision and computational power have improved vibration-based damage detection, proving efficient for online monitoring of visible surface damage, such as cracks [55] and scratches [56]. The effectiveness of these methods depends on the resolution and frame rates of the cameras. Effective damage detection methods have been developed for various structures, ranging from simple components to complex structures [57].

When applying damage detection to AMMs, an immediate challenge is addressing production uncertainties [58,59], which are particularly relevant for additively manufactured AMMs. These uncertainties can arise from variations in material properties [60,61] and manufacturing tolerances [62,63]. They can lead to discrepancies between the actual structure and the idealized model, resulting in false positives or negatives in detection results [64]. Moreover, measurement errors can introduce uncertainties in the identification of irregularities and abnormalities in transient and steady-state responses of AMMs, further complicating damage detection and localization. To address the challenges posed by production uncertainties and measurement errors, researchers are exploring advanced signal processing techniques, improved sensor technologies, and robust statistical methods to enhance the sensitivity and specificity of vibration-based damage detection approaches. However, there is limited understanding of how damage-sensitive modal parameters and unique structural parameters of acoustic metamaterials can be used for damage detection. Investigating the sensitivity of these parameters in locally resonant AMMs is crucial for developing more resilient and reliable metamaterial-based structures.

This work focuses on the modal sensitivity of finite locally resonant AMMs. The influence of damage on the structural dynamic properties of the AMMs is examined. Equations of motion are presented for damaged finite AMMs. The effective mass of a damaged mass-in-mass unit is formulated. Effects of stiffness changes of the external and internal springs on the effective mass are discussed. The sensitivity of the eigenvalues of the AMMs to damage is derived, and the mode shape changes caused by

damage are considered. Changes in effective mass and eigenvalues due to damage are quantified. The modal assurance criterion is employed to quantify mode shape changes caused by damage. A damage index is proposed for theoretical studies of the local effects of damage on modal deformations of internal and external springs of the AMMs. A comprehensive numerical investigation is conducted on a finite locally resonant AMM to quantitatively demonstrate the effects of a damaged mass-in-mass unit on the effective mass, frequency response functions, eigenvalues, mode shapes, and modal deformations.

The remaining part of this paper is outlined as follows. The equations of motion for the damaged finite locally resonant AMM is formulated in Section 2. Formulations to quantify the influence of damage on the effective mass and to conduct modal sensitivity analysis for AMMs are proposed in Sections 3.1 and 3.2, respectively. The numerical investigation is described and discussed in Section 4. Conclusions of this work are presented in Section 5.

2. Structural dynamics of damaged finite locally resonant AMMs

In the following section, equations of motion are derived for examining the structural dynamic properties of a damaged finite locally resonant AMM.

A one-dimensional locally resonant mass-in-mass unit consists of an internal rigid mass and an external one, and the two masses are connected by an internal linear spring . A finite locally resonant AMM is formed by N such mass-in-mass units that are connected by N-1 identical external linear springs and placed periodically with a spacing L. The AMM is shown in Fig. 1, and it has free-free boundary conditions.

The equation of motion for the *j*th external mass, which is neither the 1st nor *N*th one, can be expressed by

$$m_1^{(j)}\ddot{u}_1^{(j)} - k_1^{(j-1)}u_1^{(j-1)} + \left(k_1^{(j-1)} + k_1^{(j)} + k_2^{(j)}\right)u_1^{(j)} - k_2^{(j)}u_2^{(j)} - k_1^{(j)}u_1^{(j+1)} = f_1^{(j)}\,, \eqno(1)$$

where an overdot denotes differentiation with respect to time t, $m_1^{(j)}$ is jth external mass, $k_1^{(j)}$ and $k_2^{(j)}$ are the stiffness of the jth external and internal springs, respectively, $u_1^{(j)}$ and $u_2^{(j)}$ are the displacements of the jth external and internal masses, respectively, and $f_1^{(j)}$ is the force applied to $m_1^{(j)}$. The equations of motion of the 1st and Nth external masses are

$$m_1^{(1)}\ddot{u}_1^{(1)} + \left(k_1^{(1)} + k_2^{(1)}\right)u_1^{(1)} - k_1^{(1)}u_1^{(2)} - k_2^{(1)}u_2^{(1)} = f_1^{(1)} \tag{2}$$

and

$$m_1^{(N)} \ddot{u}_1^{(N)} - k_1^{(N-1)} u_1^{(N-1)} + \left(k_1^{(N-1)} + k_2^{(N)} \right) u_1^{(N)} - k_2^{(N)} u_2^{(N)} = f_1^{(N)}, \tag{3}$$

respectively. The equation of motion of the jth inner mass is

$$m_2^{(j)}\ddot{u}_2^{(j)} - k_2^{(j)}u_1^{(j)} + k_2^{(j)}u_2^{(j)} = f_2^{(j)},$$
 (4)

where $m_2^{(j)}$ is jth internal mass with j being an integer ranging between 1 and N, and $f_2^{(j)}$ is the force applied to $m_2^{(j)}$. Based on Eqs. (1) through (4), the equations of motions of the entire AMM can be written in a matrix form:

$$\mathbf{M}\ddot{\mathbf{x}} + \mathbf{K}\mathbf{x} = \mathbf{f} \,, \tag{5}$$

where

$$\mathbf{M} = \begin{bmatrix} \mathbf{M}_1 & \mathbf{0} \\ \mathbf{0} & \mathbf{M}_2 \end{bmatrix} \tag{6}$$

denotes the mass matrix, in which

$$\mathbf{M}_1 = \text{diag} \begin{pmatrix} m_1^{(1)} & m_1^{(2)} & \dots & m_1^{(j)} & \dots & m_1^{(N)} \end{pmatrix}$$
 (7)

is an $N \times N$ diagonal matrix,

$$\mathbf{M}_2 = \text{diag} \begin{pmatrix} m_2^{(1)} & m_2^{(2)} & \dots & m_2^{(j)} & \dots & m_2^{(N)} \end{pmatrix}$$
 (8)

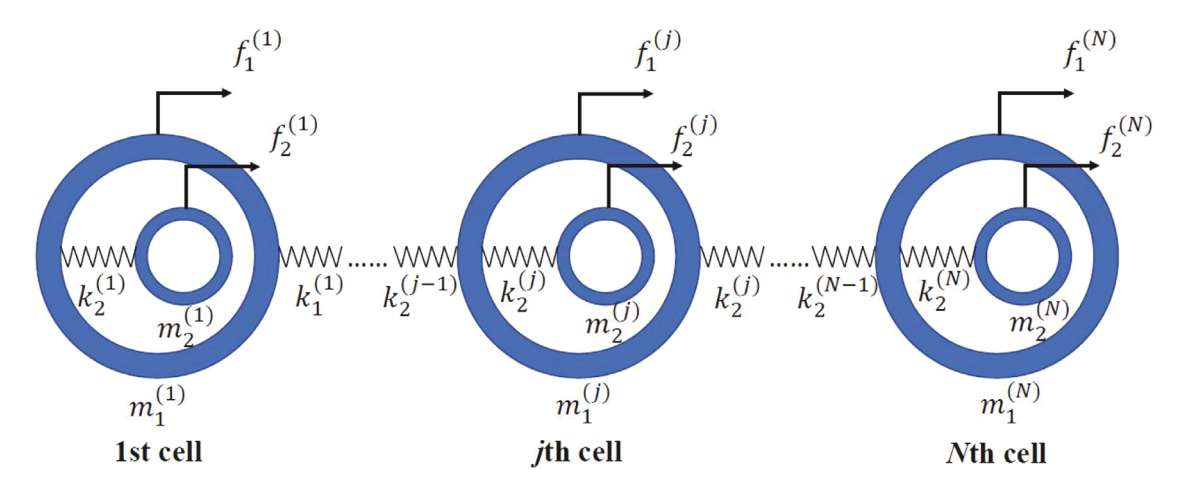


Fig. 1. Finite locally resonant AMM with N one-dimensional mass-in-mass units. The structural components of each unit, including the internal and external masses and springs, can be modified to simulate various damage scenarios.

is an $N \times N$ diagonal matrix and **0** denotes an $N \times N$ zero matrix,

$$\mathbf{x} = \begin{bmatrix} x_1^{(1)} & x_1^{(2)} & \dots & x_1^{(N)} & x_2^{(1)} & x_2^{(2)} & \dots & x_2^{(N)} \end{bmatrix}^{\mathrm{T}}$$
(9)

denotes a 2N-dimensional displacement vector, in which the superscript $^{\rm T}$ denotes matrix transpose,

$$\mathbf{K} = \begin{bmatrix} \mathbf{K}_1 & -\mathbf{K}_2 \\ -\mathbf{K}_2 & \mathbf{K}_2 \end{bmatrix}$$
 (10)

denotes the stiffness matrix, in which

$$\mathbf{K}_{1} = \begin{bmatrix} k_{1}^{(1)} + k_{2}^{(1)} & -k_{1}^{(1)} & \dots & 0 & 0 \\ -k_{1}^{(1)} & k_{1}^{(1)} + k_{1}^{(2)} + k_{2}^{(2)} & \dots & 0 & 0 \\ \vdots & \vdots & \ddots & \vdots & \vdots \\ 0 & 0 & \dots & k_{1}^{(N-2)} + k_{1}^{(N-1)} + k_{2}^{(N-1)} & -k_{1}^{(N-1)} \\ 0 & 0 & \dots & -k_{1}^{(N-1)} & k_{1}^{(N-1)} + k_{2}^{(N)} \end{bmatrix}$$

is an $N \times N$ symmetric matrix and

$$\mathbf{K}_2 = \operatorname{diag}\left(\begin{array}{cccc} k_2^{(1)} & k_2^{(2)} & \dots & k_2^{(j)} & \dots k_2^{(N)} \end{array}\right)$$
 (12)

is an $N \times N$ diagonal matrix and

$$\mathbf{f} = \begin{bmatrix} f_1^{(1)} & f_1^{(2)} & \dots & f_1^{(N)} & f_2^{(1)} & f_2^{(2)} & \dots & f_2^{(N)} \end{bmatrix}^{\mathrm{T}}$$
 (13)

denotes a 2N-dimensional force vector. The equations of motion in Eq. (5) facilitate the manipulation of the structural parameters of the AMM and thereby the simulation of both its intact and damaged states.

The corresponding eigenvalue problem and frequency response functions are presented in Appendix A to facilitate comprehensive investigation of the structural dynamic properties of a damaged AMM.

3. Quantification of influence of structural damage on AMMs

In this section, the intact and damaged states of the AMM in Fig. 1 are defined. Formulations are provided for investigation of the influence of damage on the effective mass of a mass-in-mass unit, natural frequencies, mode shapes, and modal deformations of the AMM.

A typical intact AMM has all N identical mass-in-mass units with

$$m_1^{(j)} = m_1, (14)$$

$$m_2^{(j)} = m_2$$
, (15)

$$k_1^{(j)} = k_1,$$
 (16)

and

$$k_2^{(j)} = k_2 (17)$$

for all j, where m_1 and m_2 denote the mass of intact external and internal masses, respectively, and k_1 and k_2 denote the stiffness of intact external and internal springs, respectively. While decrease of stiffness are often resulted by the occurrence of damage to a structure in practice [51], the simultaneously resulted decrease of its mass are so small that they can be considered negligible. Hence it is assumed that only $k_{\lambda}^{(j)}$ decreases and $m_{\lambda}^{(j)}$ remains unchanged when damage occurs to the AMM in this work. A damage scenario of the jth mass-in-mass unit can be described by introducing non-dimensional structural integrity parameters $\xi_1^{(j)}$ and $\xi_2^{(j)}$ such that

$$k_1^{(j)} = \zeta_1^{(j)} k_1 \tag{18}$$

and

$$k_2^{(j)} = \zeta_2^{(j)} k_2 \,. \tag{19}$$

For the jth mass-in-mass unit, its external spring is considered intact and completely damaged when $\zeta_1^{(j)}$ is equal to 1 and 0, respectively. Similarly, its internal spring is considered intact and completely damaged when $\zeta_2^{(j)}$ is equal to 1 and 0, respectively.

3.1. Effective mass of damaged mass-in-mass unit

A mass-in-mass unit can be represented by a single mass and the concept of effective mass is discussed in Ref. [18]. The effective mass associated with a mass-in-mass unit when it is intact can be expressed by a function of ω :

$$m_{\rm eff}(\omega) = m_1 + \frac{m_2 \omega_0^2}{\omega_0^2 - \omega^2},$$
 (20)

where

$$\omega_0 = \sqrt{\frac{k_2}{m_2}} \tag{21}$$

calculates the intact local resonance frequency of m_2 . Based on Eq. (20), $m_{\rm eff}$ is not related to the value of k_1 but by those of m_1 , m_2 and k_2 . By non-dimensionalizing ω in Eq. (20) with ω_0 , one has

$$m_{\rm eff}(\bar{\omega}) = m_1 + \frac{m_2}{1 - \bar{\omega}^2},$$
 (22)

where

$$\bar{\omega} = \frac{\omega}{\omega_0} \tag{23}$$

denotes the non-dimensional frequency. When $\bar{\omega}$ approaches to 1, the value of $m_{\rm eff}$ will become unbounded. Especially, when $\bar{\omega}$ approaches to 1 from below and above, $m_{\rm eff}$ approaches to positive and negative infinite, respectively. In cases of $m_{\rm eff} < 0$ and $m_{\rm eff} \gg 1$ for a massin-mass unit, the vibration magnitude of its associated external mass will be reduced, and the reduction will become significant when $\bar{\omega} \approx 1$. Based on Eqs. (19) and (20), the effective mass of the jth mass-in-mass unit, when damage occurs and causes changes to $k_2^{(j)}$, can be expressed by

$$m_{\text{eff}}^{(j)}(\omega) = m_1 + \frac{m_2 \zeta_2^{(j)} \omega_0^2}{\zeta_2^{(j)} \omega_0^2 - \omega^2}$$
 (24)

and its non-dimensionalized form is

$$m_{\text{eff}}^{(j)}(\bar{\omega}) = m_1 + \frac{m_2 \zeta_2^{(j)}}{\zeta_2^{(j)} - \bar{\omega}^2}.$$
 (25)

The effective mass in Eqs. (24) and (25) further demonstrates that while the occurrence of damage can alter the values of $\zeta_1^{(j)}$ and $\zeta_2^{(j)}$, it only affects the effective mass when $\zeta_2^{(j)}$ changes and remains unrelated to $\zeta_1^{(j)}$. A normalized effective mass is defined by

$$\bar{m}_{\rm eff}^{(j)}(\bar{\omega}) = \frac{m_{\rm eff}^{(j)}}{m_{\rm total}},\tag{26}$$

where

$$m_{\text{total}} = m_1 + m_2 \tag{27}$$

calculates the total mass of the intact unit, and when $\bar{\omega}=0$, $\bar{m}_{\rm eff}^{(j)}=1$ for all $\zeta_{\circ}^{(j)}$.

Based on Eq. (25), the significant vibration magnitude reduction of $m_1^{(j)}$ will occur when $\bar{\omega} \approx \sqrt{\zeta_2^{(j)}}$. Further, $m_{\rm eff}^{(j)}$ and $\bar{m}_{\rm eff}^{(j)}$ can be considered to be local properties of the jth unit as their values are only determined by the internal structural parameters of the jth unit. To quantify the effects of the damage-caused reduction of $k_2^{(j)}$ on $\bar{m}_{\rm eff}^{(j)}$, the damage-caused change of $\bar{m}_{\rm eff}^{(j)}$ is defined by

$$\Delta \bar{m}_{\rm eff}^{(j)}\left(\bar{\omega}\right) = \bar{m}_{\rm eff}^{(j)}\left(\bar{\omega}\right) - \bar{m}_{\rm eff}\left(\bar{\omega}\right)\,,\tag{28}$$

where

$$\bar{m}_{\rm eff}(\bar{\omega}) = \frac{m_{\rm eff}}{m_{\rm total}} \tag{29}$$

calculates the intact normalized effective mass. The effective mass change $\Delta \bar{m}_{\rm eff}^{(j)}$ is a function of \bar{o} , and a non-zero $\Delta \bar{m}_{\rm eff}^{(j)}$ can void the typical definition of a bandgap for the AMM in its intact state, where magnitudes of elastic waves decrease with constant frequency-dependent decay rates. However, $\Delta \bar{m}_{\rm eff}^{(j)}$ is locally confined to the jth damaged unit and its impact on the overall vibration reduction and elastic wave suppression functionalities can be limited. However, it is worth investing its effects on the vibration parameters of the AMM through modal sensitivity analysis.

3.2. Modal sensitivity analysis

3.2.1. Sensitivity of natural frequencies

When damage occurs and cause decrease of stiffness of the springs of the AMM, a non-zero variation $\delta \mathbf{K}$ is introduced to \mathbf{K} in the eigenvalue problem in Eq. (A.1) and it leads to variations of ω_k^2 and ϕ_k that are denoted by $\delta \omega_k^2$ and $\delta \phi_k$, respectively. The eigenvalue problem of such a damaged AMM can be expressed by [65]

$$\left[\mathbf{K} + \delta \mathbf{K} - \mathbf{M} \left(\omega_k^2 + \delta \omega_k^2\right)\right] \left(\boldsymbol{\phi}_k + \delta \boldsymbol{\phi}_k\right) = \mathbf{0}. \tag{30}$$

Expanding and rearranging Eq. (30) yield

$$(\mathbf{K} - \omega_k^2 \mathbf{M}) \, \boldsymbol{\phi}_k + \delta \mathbf{K} \, (\boldsymbol{\phi}_k + \delta \boldsymbol{\phi}_k) - \delta \omega_k^2 \mathbf{M} \, (\boldsymbol{\phi}_k + \delta \boldsymbol{\phi}_k) + (\mathbf{K} - \omega_k^2 \mathbf{M}) \, \delta \boldsymbol{\phi}_k = \mathbf{0} \,.$$
(31)

Based on Eq. (A.1) and

$$\boldsymbol{\phi}_{k}^{\mathrm{T}} \left(\mathbf{K} - \omega_{k}^{2} \mathbf{M} \right) \delta \boldsymbol{\phi}_{k} = \mathbf{0}, \tag{32}$$

pre-multiplying both sides of Eq. (31) by ϕ_k^{T} yields

$$\boldsymbol{\phi}_{k}^{\mathrm{T}} \delta \mathbf{K} \left(\boldsymbol{\phi}_{k} + \delta \boldsymbol{\phi}_{k} \right) - \boldsymbol{\phi}_{k}^{\mathrm{T}} \delta \omega_{k}^{2} \mathbf{M} \left(\boldsymbol{\phi}_{k} + \delta \boldsymbol{\phi}_{k} \right) = \mathbf{0}.$$
 (33)

Eq. (33) can be written as

$$\boldsymbol{\phi}_{k}^{\mathrm{T}} \delta \mathbf{K} \widetilde{\boldsymbol{\phi}}_{k} = \delta \omega_{k}^{2} \boldsymbol{\phi}_{k}^{\mathrm{T}} \mathbf{M} \widetilde{\boldsymbol{\phi}}_{k} , \qquad (34)$$

where

$$\widetilde{\boldsymbol{\phi}}_{k} = \boldsymbol{\phi}_{k} + \delta \boldsymbol{\phi}_{k} \tag{35}$$

denotes the kth damaged mode shape vector. The vector $\widetilde{\pmb{\phi}}_k$ can be normalized such that

$$\boldsymbol{\phi}_k^{\mathrm{T}} \mathbf{M} \widetilde{\boldsymbol{\phi}}_k = 1 \tag{36}$$

and Eq. (34) becomes

$$\boldsymbol{\phi}_k^{\mathrm{T}} \delta \mathbf{K} \widetilde{\boldsymbol{\phi}}_k = \delta \omega_k^2 \,. \tag{37}$$

In many current vibration-based damage identification works, it has been a commonly accepted assumption that $\delta \phi_k \approx 0$, i.e., $\widetilde{\phi}_k \approx \phi_k$, which is, however, false for the AMM. When an internal spring of a unit is damaged, decreasing the value of $\zeta_2^{(J)}$, $\Delta \bar{m}_{\rm eff}^{(J)}$ in Eq. (28) can be extremely large values at certain frequencies. Such large changes of $\bar{m}_{\rm eff}$ can introduce abrupt non-negligible changes to mode shapes of the AMM associated with the frequencies aligning with those of $\Delta \bar{m}_{\rm eff}^{(J)}$.

Based on Eqs. (37) and (A.3), the percentage relative change of the kth natural frequency [66,67] of the AMM due to damage is defined by

$$r_k = \frac{\sqrt{\omega_k^2 + \delta \omega_k^2} - \omega_k}{\omega_k} \times 100\% = \left(\sqrt{1 + \frac{\delta \omega_k^2}{\omega_k^2}} - 1\right) \times 100\%.$$
 (38)

The value of r_k ranges between 0% and 100%, and it is capable of indicating occurrence of damage and quantifying the influence of the damage on ω_k in a relative sense. Further, when plotted as a function of $\bar{\omega}$, it inspects the relation between values of the natural frequency changes and their closeness to bandgaps or other specific frequency ranges. For the same damage severity at different spring elements, a higher value of r_k indicates that the kth mode is more sensitive to the damage, while a smaller value of r_k indicates the opposite.

3.2.2. Sensitivity of mode shapes and modal deformations of springs

The sensitivity of ω_k to damage at certain location is consistent with that mode shapes. To quantify the overall effects of damage on the kth mode shape, the modal assurance criterion (MAC) is used, which can be expressed by [68]

$$MAC_{k} = \frac{\left(\boldsymbol{\phi}_{k}^{H} \widetilde{\boldsymbol{\phi}}_{k}\right)^{*} \left(\boldsymbol{\phi}_{k}^{H} \widetilde{\boldsymbol{\phi}}_{k}\right)}{\left(\boldsymbol{\phi}_{k}^{H} \boldsymbol{\phi}_{k}\right) \left(\widetilde{\boldsymbol{\phi}}_{k}^{H} \widetilde{\boldsymbol{\phi}}_{k}\right)} \times 100\%,$$
(39)

where the superscripts * and ^H denote complex conjugation and Hermitian transpose, respectively. The value of MAC $_k$ ranges from 0% to 100%, and MAC $_k$ quantifies the similarity between ϕ_k and $\widetilde{\phi}_k$: the higher the value of MAC $_k$ the more similar the two mode shapes are. Its values 0% and 100% indicate that the two mode shapes are orthogonal and completely correlated, respectively. Note that MAC $_k$ quantifies the overall effects of damage on mode shapes rather than local effects of the damage.

Inspection of local effects of the damage on ϕ_k can be achieved by point-by-point comparisons between modal deformations of the springs associated with ϕ_k and $\widetilde{\phi}_k$. When the AMM is intact, the modal deformation of the jth intact external and internal springs associated with the kth mode are defined as

$$\Delta\phi_{1,k}^{(j)u} = \phi_{1,k}^{(j)} - \phi_{1,k}^{(j-1)} \tag{40}$$

and

$$\Delta \phi_{2k}^{(j)u} = \phi_{2k}^{(j)} - \phi_{1k}^{(j)}, \tag{41}$$

respectively. A modal deformation damage index is defined based on modal deformations of each spring, and it is expressed by

$$\eta_{\lambda,k}^{(j)} = \frac{\left| \Delta \phi_{\lambda,k}^{(j)d} - \Delta \phi_{\lambda,k}^{(j)u} \right|}{\max_{j=1,2,\dots,n,\gamma=1,2} \left| \Delta \phi_{\lambda,k}^{(j)u} \right|},\tag{42}$$

where $\Delta \phi_{\lambda,k}^{(j)d}$ denotes the modal deformation of the *j*th damaged external or internal spring associated with the *k*th mode, in which

$$\Delta\phi_{1,k}^{(j)d} = \widetilde{\phi}_{1,k}^{(j)} - \widetilde{\phi}_{1,k}^{(j-1)} \tag{43}$$

and

$$\Delta \phi_{2k}^{(j)d} = \widetilde{\phi}_{2k}^{(j)} - \widetilde{\phi}_{1k}^{(j)}, \tag{44}$$

and $j=1,2,\ldots,n,\gamma=1,2\max\left|\Delta\phi_{\lambda,k}^{(j)u}\right|$ calculates the maximum absolute entry of the kth modal deformation of the spring when the AMM is intact. The value of $\eta_{\lambda,k}^{(j)}$ in Eq. (42) is non-negative and ranges from 0 to 1. It quantifies the influence of the damage on mode shapes in a spring-by-spring manner and the sensitivity of the defamation of each spring to the damage. While some AMM elements in a structure may not be accessible for displacement/deformation measurements, $\eta_{\lambda,k}^{(j)}$ is not suitable for damage identification but ideal for localizing effects of damage on a mode shape for theoretical study purposes.

4. Numerical investigation

In the following section, a comprehensive numerical investigation is presented to elucidate the quantitative influence of damage on the AMM using the formulations provided in Section 3. An intact finite AMM with N=20 identical mass-in-mass units is simulated with $m_1=10$ kg, $m_2=4$ kg, $k_1=60$ GN/m, $k_2=6$ GN/m and L=0.1 m; the local resonance frequency is calculated to be $\omega_0=3.87\times 10^4$ rad/s using Eq. (21). Three damage scenarios are introduced to the AMM by reducing $\zeta_2^{(7)}$ to 98%, 90%, and 70%, simulating damage ranging from minor to medium severities.

4.1. Dispersion analysis and damage influence on effective mass

An infinitely long AMM consisting of the above described intact mass-in-mass units is first considered for harmonic wave propagation and estimation of the bandgap of the finite AMM. As a major feature of the infinite AMM, the bandgap exists within which harmonic waves with certain frequencies are blocked from propagation. The lower and upper limits of the bandgap can be calculated by [69]

$$\bar{\omega} = \frac{1}{\sqrt{2}} \sqrt{\left(1 + \frac{m_2}{m_1} + \frac{4m_2k_1}{m_1k_2}\right) - \sqrt{\left(1 + \frac{m_2}{m_1} + \frac{4m_2k_1}{m_1k_2}\right)^2 - \frac{16m_2k_1}{m_1k_2}}}$$
(45)

and

$$\bar{\omega} = \sqrt{1 + \frac{m_2}{m_1}},\tag{46}$$

respectively. The values of the lower and upper limits of the infinite AMM are calculated to be $\bar{\omega}=0.9869$ and $\bar{\omega}=1.1832$, respectively. Note that at the upper limit of the bandgap one has $m_{\rm eff}^{(j)}=0$ but at

the lower limit of the bandgap $m_{\rm eff}^{(j)} \neq 0$. The complete derivation for the dispersion relation associated with an infinite AMM is provided in Appendix B. The band structure of the infinite AMM is plotted in Fig. 2 as a complex-valued function of $\bar{\omega}$:

$$qL(\bar{\omega}) = \alpha + j\beta. \tag{47}$$

At the lower and upper limits of the bandgap, the values of $\cosh(qL)$ in Eq. (B.19) are equal to -1 and 1, respectively. Within the identified bandgap, one has $|\cosh(qL)| > 1$ that gives $\alpha > 0$ and $\beta = 0$ or π . With $\alpha > 0$, a propagating harmonic wave of a frequency within the bandgap is suppressed and eventually blocked from propagation in the AMM as the absolute value of h in Eqs. (B.3) and (B.4) increases.

When all the mass-in-mass units are intact, the rate of the elastic wave suppression is constant and proportional to the value of α throughout the infinite AMM. The rate determines the distance by which a wave of a frequency within the bandgap can propagate before its magnitude becomes zero or negligibly small. When a unit is intact, $m_{\rm eff}^{(j)}$ is calculated using Eq. (22) and plotted in Fig. 3(a). One mechanism for the decay is the existence of negative $m_{\text{eff}}^{(j)}$ [18]. When $m_{\text{eff}}^{(j)} < 0$ the acceleration of the effective single mass representing the *j*th unit is in the opposite direction of its net applied force according to the Newton's second law of motion, and the magnitude of its displacement, which can be represented by $u_1^{(j)}$, will be reduced; the higher the value of $\left|m_{\rm eff}^{(j)}\right|$ the larger the reduction of the magnitude. Unlike an intact infinite AMM, a bandgap cannot be defined for a damaged finite AMM based on the dispersion analysis of a unit, since damaged units are different from an intact unit, which in effect breaks the assumed periodicity of the units of the infinite AMM. This is consistent with the discussion regarding $\Delta \bar{m}_{\rm eff}^{(j)}$ in Section 3.1.

When its 7th unit is damaged under the three scenarios, $\bar{m}_{eff}^{(7)}$ is plotted in Fig. 3 and compared with that of the corresponding intact unit. The three damaged $\bar{m}_{\rm eff}^{(7)}$ have a pattern similar to the intact $\bar{m}_{\rm eff}^{(j)}$. Compared with the intact $\bar{m}_{\rm eff}^{(j)}$, both the lower and upper bounds of the ranges of $\bar{\omega}$ within which the $\bar{m}_{\rm eff}^{(7)} < 0$ simultaneously change to lower values, and the quantitative changes depend on the severity of the damage, as shown in Fig. 3(b). Besides, significant increases of $m_{\text{off}}^{(7)}$ can be identified within the neighborhood of the lower bound of the bandgap associated with the intact AMM due to the occurrence of the damage, as shown in Fig. 3(c). For the damaged unit, when $\bar{\omega}$ is smaller than the lower bound of $\bar{\omega}$ for negative $\bar{m}_{\rm eff}^{(7)}$, the larger the value of $\bar{\omega}$, the larger increases of $m_{\rm eff}^{(7)}$; when $\bar{\omega}$ is larger than the upper bound of $\bar{\omega}$ for negative $\bar{m}_{\rm eff}^{(7)}$, the smaller the value of $\bar{\omega}$, the larger decrease of $m_{\rm eff}^{(7)}$. A severer damage corresponds to a wider frequency range within which non-negligible changes of $m_{\rm eff}^{(j)}$ exists. These damage-caused frequency-dependent features of $m_{\rm eff}^{(j)}$, can introduce frequency-dependent changes to vibration characteristics of the AMMs. More importantly, significant changes of the characteristics can be expected in frequencies where the value of $\Delta \bar{m}_{\rm eff}^{(j)}$ is large.

4.2. Influence on frequency response functions

When the finite AMM is intact and damaged in the three scenarios, associated end-to-end frequency response functions, denoted by $h_{(20)1,(1)1}$, are calculated using Eq. (A.4) and plotted in Fig. 4(a). The frequency response function $h_{(20)1,(1)1}$ corresponds to the dynamic output-to-input relation between the external masses of the last and first units. The magnitudes of the damaged $h_{(20)1,(1)1}$ drastically decrease within the band gap associated with an intact unit, compared with those of the intact $h_{(20)1,(1)1}$.

At frequencies beyond but close to the edges of bandgap, the influence of the damage on $h_{(20)1,(1)1}$ is identified. An enlarged view of $h_{(20)1,(1)1}$ at frequencies between $\bar{\omega}=0.975$ and $\bar{\omega}=0.99$ is shown in Fig. 4(b). At frequencies other than those near the magnitude peaks, the magnitude floor of $h_{(20)1,(1)1}$ of a damaged AMM is generally lower than that of the intact AMM. Further, the magnitude peaks of $h_{(20)1,(1)1}$ are

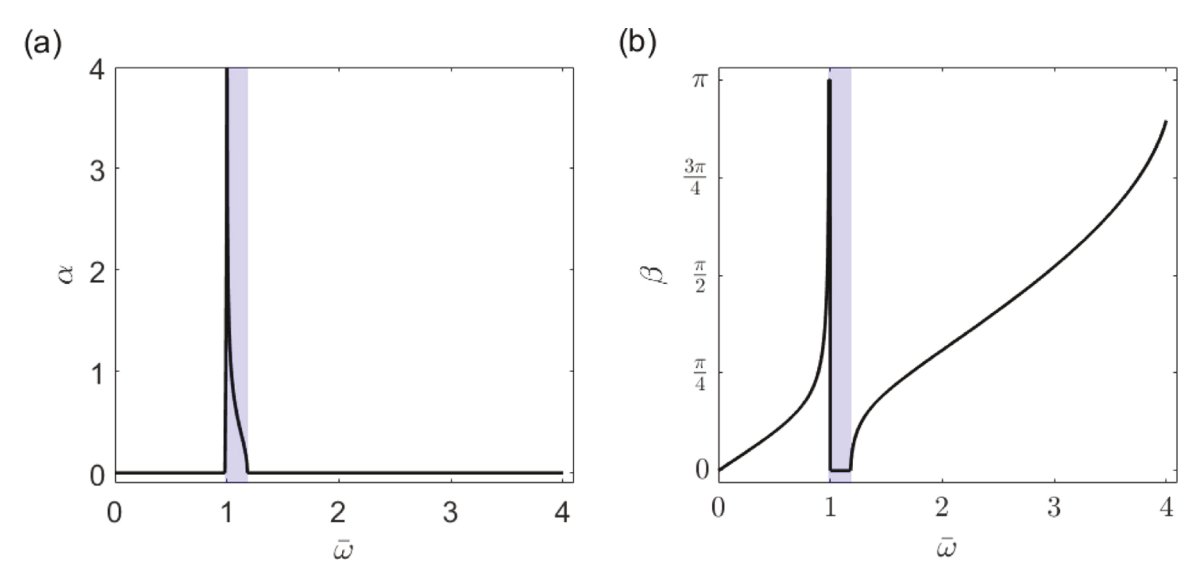


Fig. 2. Band structure of the mass-in-mass unit, showing the real (a) and imaginary (b) parts obtained from the dispersion relation given in Eq. (B.19). The bandgap is represented by the frequency range in which a non-zero α value exists, and it is highlighted as a shaded area.

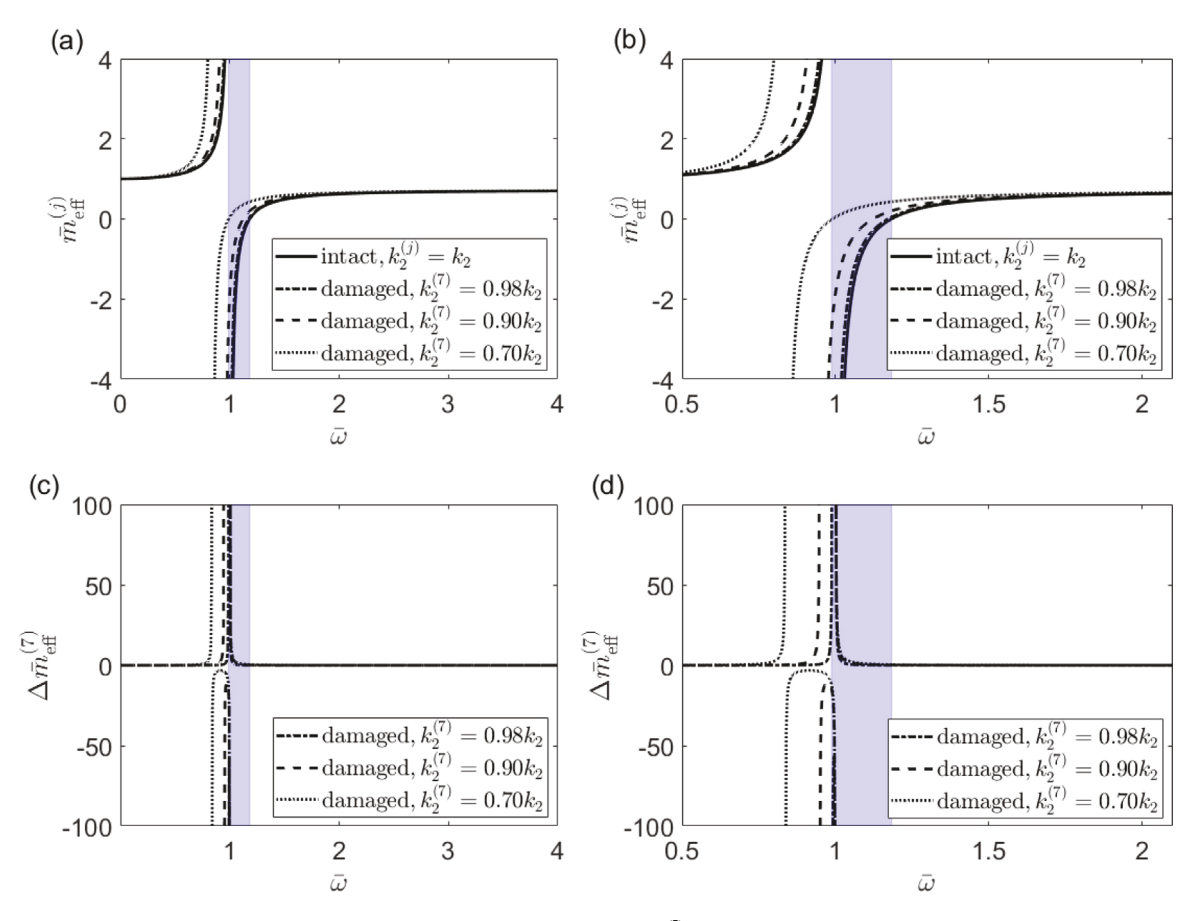


Fig. 3. Effects of damage on the mass-in-mass unit in the AMM. (a) Normalized effective mass $\bar{m}_{\rm eff}^{(7)}$ of the intact mass-in-mass unit and the 7th unit with damage corresponding to $k_2^{(7)} = \zeta_2^{(7)} k_2$, where $\zeta_2^{(7)} = 0.98$, 0.90, and 0.70. (b) Enlarged view of $\bar{m}_{\rm eff}^{(f)}$ of the intact mass-in-mass unit and the 7th unit with damage shown in (a). (c) Changes of effective mass $\Delta \bar{m}_{\rm eff}^{(7)}$ due to the structural damage, and (d) an enlarged view of $\Delta \bar{m}_{\rm eff}^{(7)}$ shown in (c). The bandgap associated with the intact unit is highlighted as a shaded area.

shifted to lower frequencies, which indicates the natural frequencies of the acoustic modes are lowered due to the occurrence of the damage, which will be further discussed in Section 4.3.1. An enlarged view of $h_{(20)1,(1)1}$ between $\bar{\omega}=0.5$ and $\bar{\omega}=0.975$ is shown in Fig. 4(c). The differences among intact and damaged $h_{(20)1,(1)1}$ gradually diminish as

 $\bar{\omega}$ approaches to $\bar{\omega}=0.5,$ and they become less noticeable when $\bar{\omega}$ approaches to 0.

An enlarged view of $h_{(20)1,(1)1}$ between $\bar{\omega}=1.16$ and $\bar{\omega}=1.26$ is shown in Fig. 4(d). When the AMM is damaged, the first magnitude peak at the natural frequency that is higher than the higher edge of the

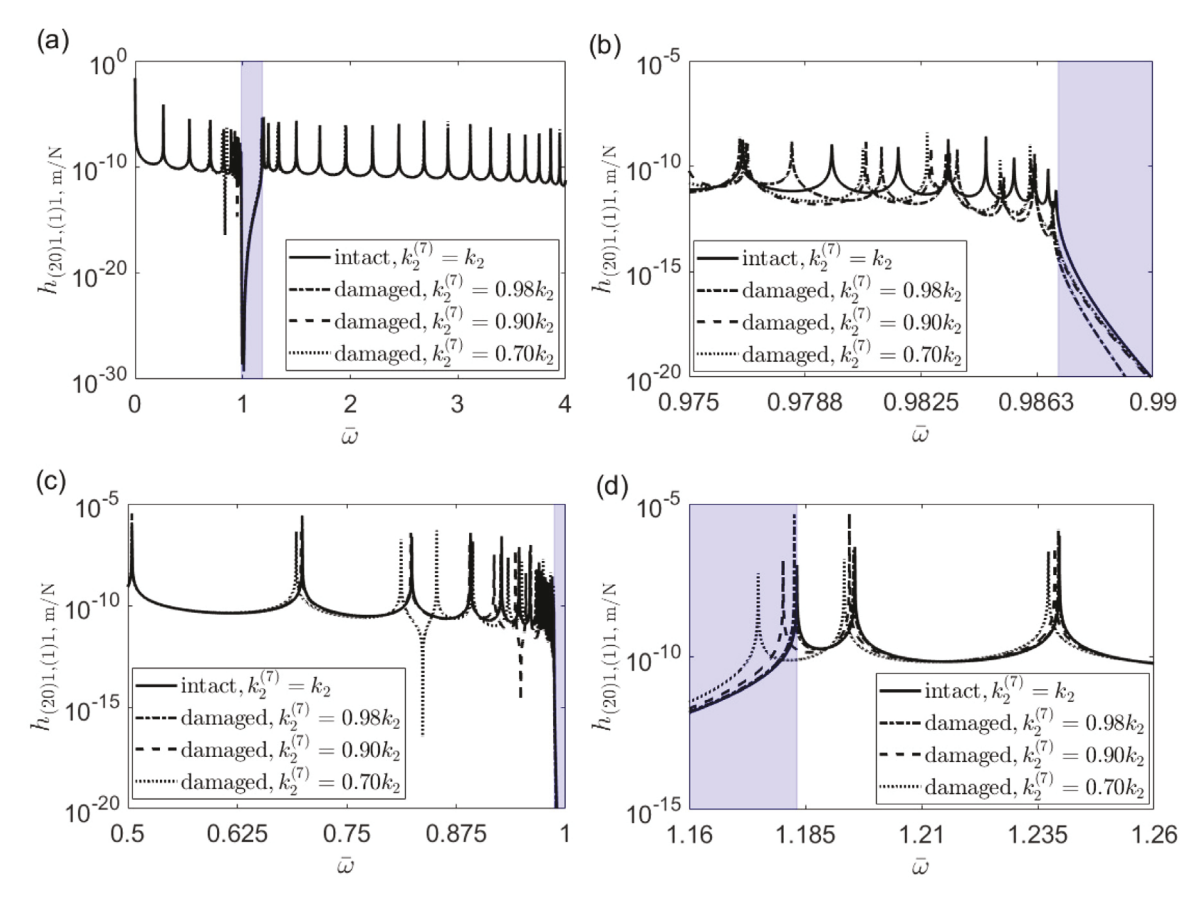


Fig. 4. Effects of damage on the end-to-end frequency response function $h_{(20)1,(1)1}$ of the AMM. (a) Magnitudes of $h_{(20)1,(1)1}$ for both intact and damaged AMM. (b) Enlarged view of (a) highlighting significant damage effects at frequencies near the lower edge of the bandgap, between $\bar{\omega} = 0.975$ and 0.99. (c) Enlarged view of (a) illustrating diminishing damage effects at frequencies ranging from $\bar{\omega} = 1$ to 0.5. (d) Enlarged view of (a) displaying less significant damage effects at frequencies near the upper edge of the bandgap, between $\bar{\omega} = 1.16$ and 1.26. The bandgap associated with the intact unit is highlighted as a shaded area.

bandgap is shifted to lower frequencies and enters the bandgap. The third magnitude peak at the natural frequency higher than the higher edge of the bandgap is also shifted due to the damage. Though similar shifts occurs to magnitude peaks corresponding to other magnitude peaks, the frequency changes of the shifts become smaller and smaller as $\bar{\omega}$ increases.

The influences of damage on the frequency response functions directly correspond to $\Delta\bar{m}_{\rm eff}^{(7)}$ in Fig. 3. This derives from the consistency that the larger the value of $\Delta\bar{m}_{\rm eff}^{(7)}$, the greater the impact on the frequency response function in Fig. 4. Conversely, the smaller the value of $\Delta\bar{m}_{\rm eff}^{(7)}$, the less the changes in the frequency response function. The latter is evident in $h_{(20)1,(1)1}$ with $\bar{\omega} \geq 2$: nearly no changes in the frequency response functions can be seen, which aligns with $\Delta\bar{m}_{\rm eff}^{(7)}$ in the same frequency range.

4.3. Influence on modal parameters

4.3.1. Influence on natural frequencies

Natural frequencies of the elastic modes of the intact and damaged AMMs are calculated by solving the eigenvalue problem in Eq. (A.1), based on which benchmark $\delta\omega_k^2$ associated with $\zeta_2^{(7)}=0.98$ and $\zeta_2^{(7)}=0.70$ are obtained and plotted in Fig. 5(a) and (b), respectively. The changes of eigenvalues are then calculated as $\phi_k^H \delta \mathbf{K} \widetilde{\phi}_k$ using Eq. (37) and plotted in Fig. 5(a) and (b), and they compare well with the benchmark ones, and this comparison verifies Eq. (37). In most existing damage identification works, the assumption that $\phi_k = \widetilde{\phi}_k$ can be proved false for the finite AMMs by calculating $\phi_k^H \delta \mathbf{K} \phi_k$ and plotted in Fig. 5(a) and (b). Certain $\phi_k^H \delta \mathbf{K} \phi_k$ values do not compare well with

the benchmark $\delta\omega_k^2$ and $\boldsymbol{\phi}_k^{\rm H}\delta\mathbf{K}\widetilde{\boldsymbol{\phi}}_k$, indicating that $\widetilde{\boldsymbol{\phi}}_k$ does not well approximate $\boldsymbol{\phi}_k$ at the certain modes.

The influence of the damage on the natural frequencies can be further understood by inspecting r_k , and it is calculated using Eq. (38) and plotted as a function of $\bar{\omega}$ in Fig. 5(c). For the same damage scenario, relatively large r_k values cluster in the neighborhoods of the bandgap of the intact AMM, and smaller r_k values are found when $\bar{\omega}$ is farther away from the bandgap. In addition, a severer damage yields a larger r_k value as indicated in Fig. 5(c) and (d). These observations generally align with $\Delta \bar{m}_{\rm eff}^{(7)}$: the closer to the bandgap, the larger the changes, though some r_k do not monotonically decrease as $\bar{\omega}$ deviates from the bandgap. Such inconsistency derives from the fact that the sensitivity of the elastic modes to the damage at a unit is inconsistent and the inconsistency depends on the location of the damage [70].

4.3.2. Influence on mode shapes and modal deformations

Mode shapes associated with the elastic modes of the intact and damaged finite AMMs are obtained from the solutions to their respective eigenvalue problems. The mode shapes of their 4th and 14th elastic modes, denoted by ϕ_4 and ϕ_{14} , respectively, are shown in Fig. 6. Antisymmetry of ϕ_4 and ϕ_{14} can be observed for $m_1^{(j)}$ and $m_2^{(j)}$ with respect to its middle point, and the anti-symmetry [71], for the mode shapes in this work, can be expressed by

$$\phi_{k,(j)\lambda} = -\phi_{k,(N-j+1)\lambda} \tag{48}$$

with k=4 or 14 and $1 \le j \le \left\lfloor \frac{N}{2} \right\rfloor$; N=20 for the finite AMM. When the damage occurs, no noticeable difference can be identified by comparing ϕ_4 and the corresponding one of the damaged AMM, denoted by $\widetilde{\phi}_4$, as shown in Fig. 6(a) and (c). However, significant differences can be

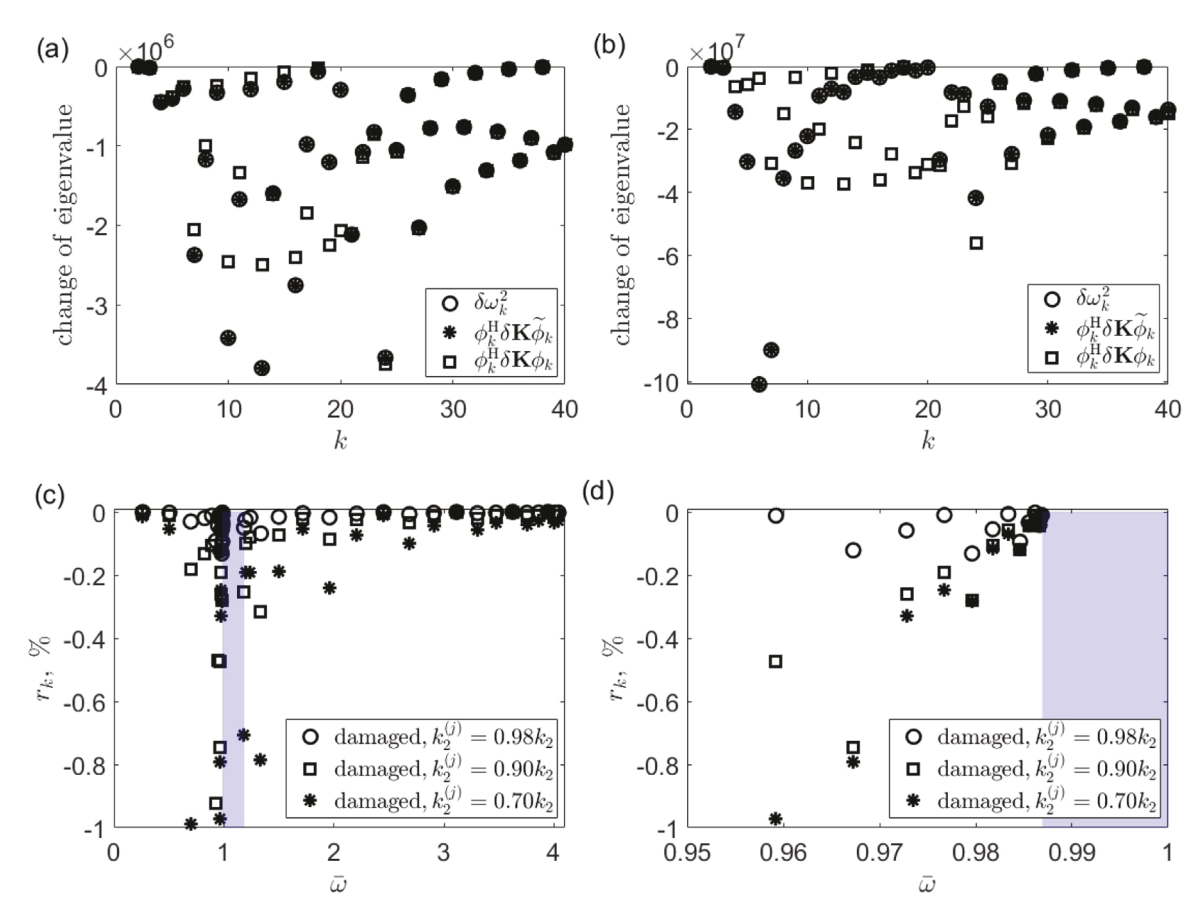


Fig. 5. Effects of damage on eigenvalues and natural frequencies of the AMM. (a) Changes in eigenvalues of the AMM for $\zeta_2^{(7)} = 0.98$, and (b) changes in eigenvalues for $\zeta_2^{(7)} = 0.70$. (c) Relative changes in natural frequencies of the damaged AMM as a function of $\bar{\omega}$, highlighting that the impact of damage is most significant near the bandgap. (d) Enlarged view of (c), illustrating that the effects of damage increase with greater damage severity. The bandgap associated with the intact AMM is highlighted as a shaded area in (c) and (d)

observed by comparing ϕ_{14} in Fig. 6(b) and the corresponding one of the damaged AMM, denoted by $\widetilde{\phi}_{14}$ in Fig. 6(d): the anti-symmetry is voided, and more importantly, significant differences of $\widetilde{\phi}_{14}$ exist in $\phi_{14,(j)\lambda}$ with $j \in [1,7]$. The effects of the damage on ϕ_4 and ϕ_{14} are different mainly because changes of $m_{\rm eff}^{(7)}$ due to the damage depend on ω , since ω_4 and ω_{14} are far beyond and close to the bandgap, respectively. Similar observations can be made for some other mode shapes: mode shapes associated with natural frequencies that are far beyond and close to the bandgap display insignificant and significant changes due to the damage, respectively.

MAC values between ϕ_k and $\widetilde{\phi}_k$ corresponding to the intact and damaged AMMs are calculated using Eq. (38) and plotted in Fig. 5. In Fig. 7(a), it can be observed that the occurrence of the damage significantly affects the mode shapes of the 6th through 20th elastic modes. As shown in Fig. 7(b), the mode shapes associated with natural frequencies close to the lower bound of the bandgap are affected to a noticeable extent due to the damage. However, the mode shapes associated with natural frequencies close to the higher bound of the bandgap are not significantly affected. These observations are inconsistent with those regarding the affects of the damage on the natural frequencies shown in Fig. 5(c). By comparing r_k in Fig. 5(c) and MAC in Fig. 7(b), it can be observed that r_k is less indicative to the occurrence of the damage than MAC, as the former has significantly smaller values than those of the latter. However, the latter usually requires extensive measurements that could be less feasible in practice.

The damage indexes $\eta_{\lambda,k}^{(j)}$ associated with ϕ_4 and ϕ_{14} of the AMM with $\zeta_2^{(7)}=0.90$ are calculated using Eq. (42) and plotted in Fig. 8(a) and (b), respectively. It can be seen that the location of the damage can be directly identified based on $\eta_{\lambda,4}^{(j)}$ where the largest index value exists

at the entry corresponding to $k_2^{(7)}$ while $\eta_{\lambda,k}^{(j)}$ corresponding to other springs remain relatively small. However, the location of the damage cannot be easily identified based on $\eta_{\lambda,14}^{(j)}$ though the damage has an larger impact is observed on the MAC value corresponding to the mode shape than that corresponding to the 14th mode shape. Though $\eta_{\lambda,14}^{(j)}$ cannot indicate the location of the damage, one can witness the local effect of the damage by identifying the location where an abrupt change of the 14th mode shape occurs, i.e., at $m_2^{(7)}$.

5. Conclusions

This paper presents a thorough examination of the modal sensitivity of finite acoustic metamaterials (AMMs) composed of periodic locally resonant mass-in-mass units when subjected to damage. These findings formulate a unique perspective to understanding the dynamic structural properties of damaged AMMs. This work first derives the equations of motion for damaged AMMs, and it introduces a novel framework for quantitatively analyzing the damage effects on the effective mass of a damaged mass-in-mass unit, considering changes in the stiffness of the internal and external springs. The effective mass is analytically shown to be influenced by the changes in stiffness of the internal spring rather than its external counterpart. This work inspects the sensitivity of the eigenvalues and mode shapes to damage using the modal assurance criterion.

Additionally, this work presents a comprehensive numerical investigation of a finite damaged AMM. It is demonstrated that the frequency response functions, eigenvalues, and mode shapes of the AMM can display significant changes at frequencies near its bandgap. As frequencies deviate from the bandgap, these changes are shown to gradually

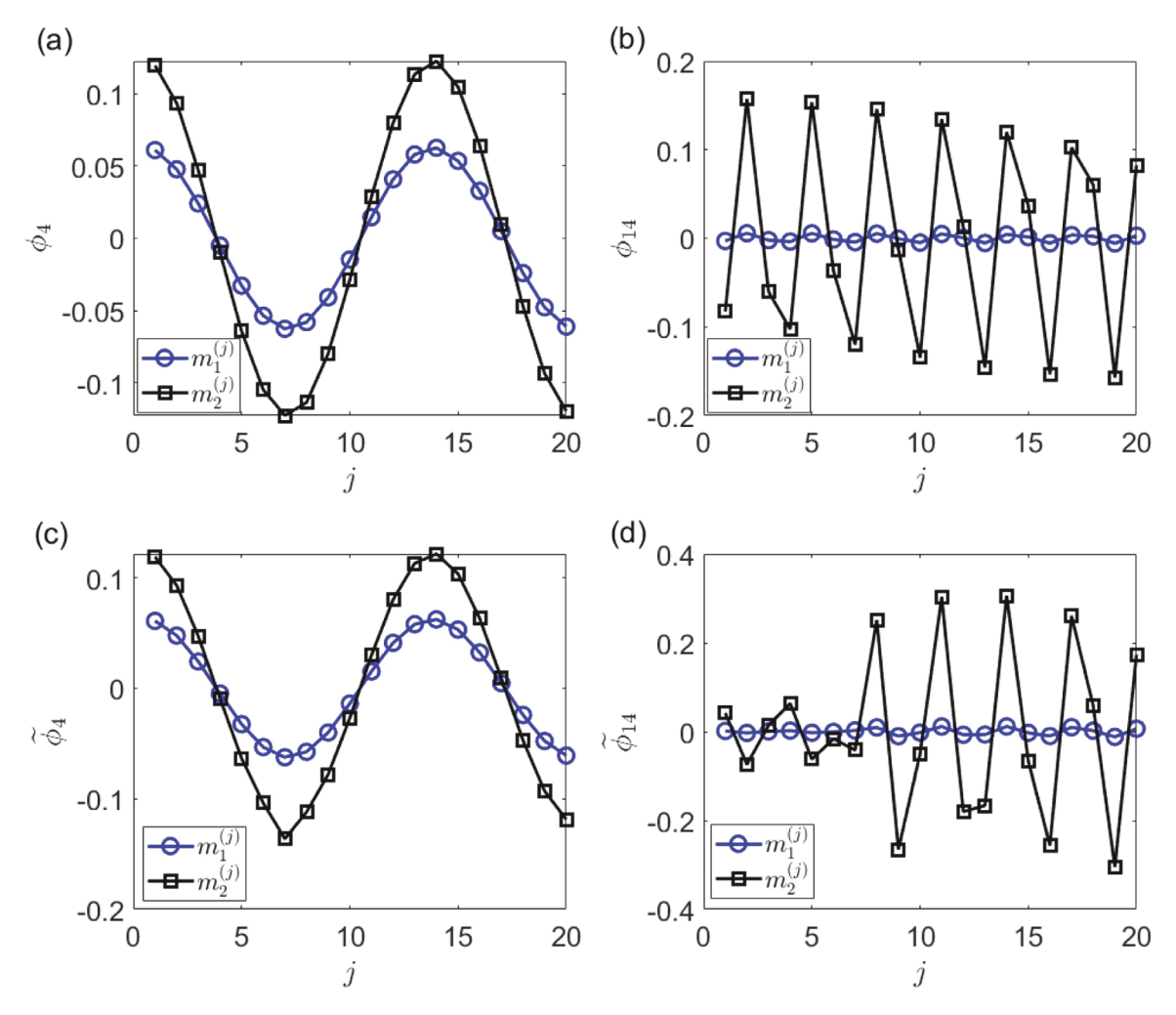


Fig. 6. Effects of damage on mode shapes of the AMM. Normalized mode shapes of the 4th mode in the (a) intact and (b) damaged AMMs. Normalized mode shapes of the 14th mode in the (c) intact and (d) damaged AMMs. The 4th mode shapes appear similar in both intact and damaged AMMs, suggesting that this mode is insensitive to damage. Conversely, the 14th mode shapes differ with the loss of anti-symmetry in the damaged mode shape, indicating a high sensitivity to damage.

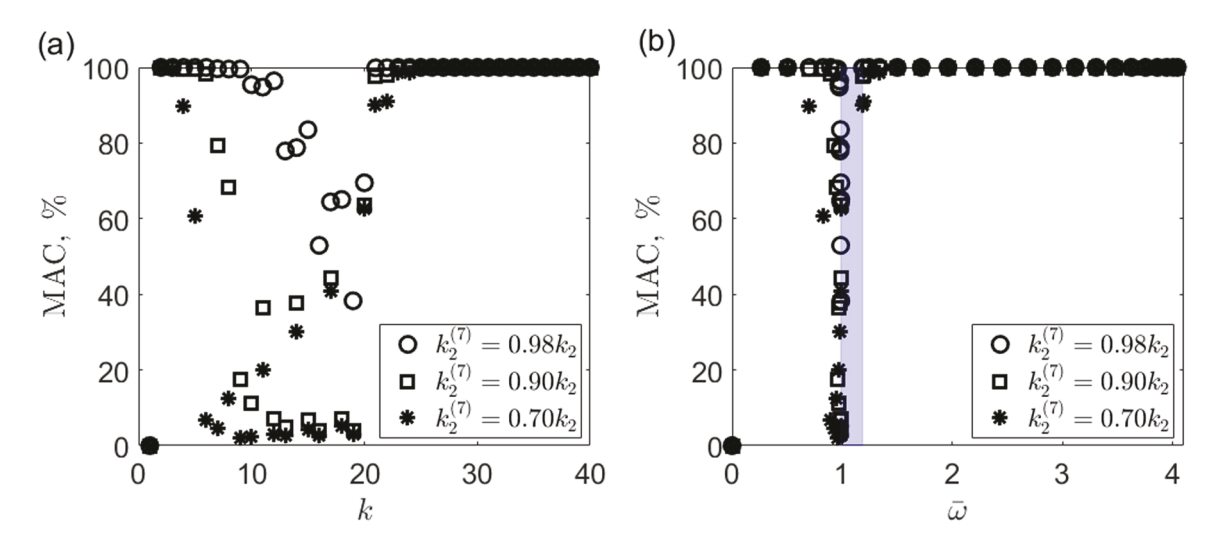


Fig. 7. Effects of damage on MAC values between the mode shapes of the intact AMM and those of the damaged AMM. MAC values plotted as functions of (a) k and (b) \bar{o} . The MAC values reveal that the effects of damage are more significant for modes in the range of the 10th to 20th modes in (a), and for modes with natural frequencies near the lower edge of the bandgap in (b). The bandgap associated with the intact unit is highlighted as a shaded area in (b).

diminish, which reaffirms the role of the frequency-dependent effective mass of a damaged mass-in-mass unit. Moreover, it reveals that significant disruptions can occur to the symmetry or anti-symmetry

inherent in a mode shape of an intact AMM due to damage. The severity of this disruption is directly related to the proximity of the natural frequency associated with the mode shape to the bandgap,

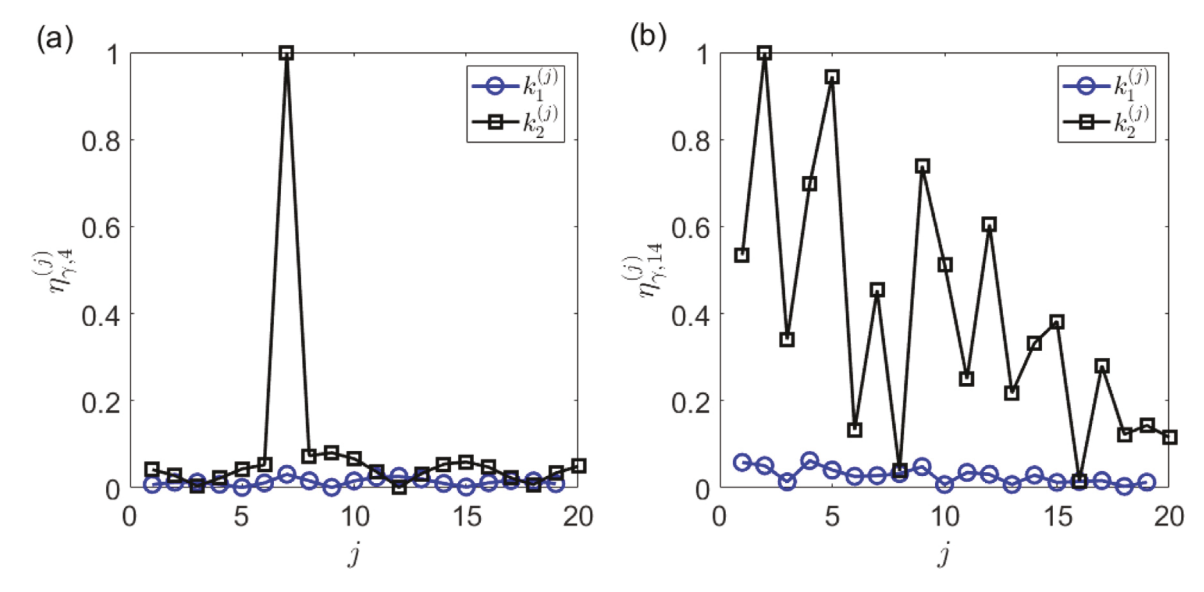


Fig. 8. Effects of damage on modal deformation of the AMM. The modal deformation damage indexes associated with (a) ϕ_4 and (b) ϕ_{14} are depicted for the AMM with $\zeta_2^{(7)} = 0.90$. While ϕ_4 exhibits less sensitivity to the damage, its modal deformation damage index better indicates the location of the damage compared to that of ϕ_{14} .

providing valuable insights into the dynamic effects of damage on such AMMs. All these observations, along with the analysis framework, establish a foundational understanding of the effects of damage on the structural dynamic properties of AMMs and device the development of effective damage identification techniques for structures incorporating metamaterials. This work contributes to the field of structural dynamics of damaged metamaterials and could lead to more resilient and reliable metamaterial-based structures across a wide array of applications.

CRediT authorship contribution statement

Y.F. Xu: Conceptualization, Methodology/Study design, Software, Validation, Formal analysis, Investigation, Resources, Data curation, Writing – original draft, Writing – review & editing, Visualization, Supervision, Project administration, Funding acquisition. G.L. Huang: Conceptualization, Writing – original draft, Writing – review & editing, Funding acquisition.

Declaration of competing interest

The authors declare that they have no known competing financial interests or personal relationships that could have appeared to influence the work reported in this paper.

Data availability

Data will be made available on request.

Acknowledgments

Xu acknowledges the support from the National Science Foundation under grant no. CMMI-1762917 and Huang acknowledges the support from the National Science Foundation under grant no. CMMI-1930873.

Appendix A

Modal parameters, including natural frequencies and mode shapes, of the AMM in Fig. 1 at its intact and damaged states can be estimated by solving an eigenvalue problem formulated using M and K in Eq. (5) [72]:

$$\left(\mathbf{K} - \mathbf{M}\omega_k^2\right) \boldsymbol{\phi}_k = \mathbf{0},\tag{A.1}$$

where ω_k^2 and ϕ_k denote the kth eigenvalue and eigenvector, respectively, and ω_k is termed as the kth circular natural frequency. An entry of ϕ_k corresponding to $m_\lambda^{(j)}$ with λ being 1 or 2 is denoted by $\phi_{k,\lambda}^{(j)}$. By mass-normalizing ϕ_k for all k, ϕ_k satisfies the orthonormality conditions that are expressed by

$$\boldsymbol{\phi}_k^{\mathrm{T}} \mathbf{M} \boldsymbol{\phi}_k = 1 \tag{A.2}$$

and

$$\boldsymbol{\phi}_{k}^{\mathrm{T}}\mathbf{K}\boldsymbol{\phi}_{k} = \omega_{k}^{2}. \tag{A.3}$$

In this work, all ϕ_k are mass-normalized using the orthogonality conditions

In experimental modal analysis, the modal parameters, including ω_k and ϕ_k are usually estimated based on measured frequency response functions. The frequency response function matrix of the AMM in Fig. 1 can be expressed using M and K in Eq. (5) [73]:

$$\mathbf{H}(\omega) = \left(\mathbf{K} - \mathbf{M}\omega^2\right)^{-1} \,, \tag{A.4}$$

where ω denote the circular frequency. An entry of **H** is denoted by $h_{(j)\lambda,(q)\gamma}$, and $h_{(j)\lambda,(q)\gamma}$ quantifies the response-to-excitation relation with $m_{\lambda}^{(j)}$ and $m_{\gamma}^{(q)}$ being the response and excitation points, respectively, in the frequency domain, where γ is an integer being equal to either 1 or 2 and q is an integer ranging between 1 and N. The entry $h_{(j)\lambda,(q)\gamma}$ (ω) can be expressed in a partial fraction form [74]:

$$h_{(j)\lambda,(q)\gamma}(\omega) = \sum_{k=1}^{N} \left(\frac{Q_k \phi_{\lambda,k}^{(j)} \phi_{\gamma,q}^{(q)}}{j\omega_k - j\omega} + \frac{Q_k^* \phi_{\lambda,k}^{(j)*} \phi_{\gamma,q}^{(q)*}}{-j\omega_k - j\omega} \right), \tag{A.5}$$

where j = $\sqrt{-1}$, Q_k is the scaling factor associated with the kth mode, and the subscript * denotes complex conjugation. When $\omega = \omega_k$, the AMM undergoes resonance, where magnitudes of $h_{(j)\lambda,(q)\gamma}$ and $u_\gamma^{(j)}$ become unbounded. With a measured $h_{(j)\lambda,(q)\gamma}$, one can estimate the value of ω_k at peaks of the magnitude plot of $h_{(j)\lambda,(q)\gamma}$ if both $\phi_{\gamma,q}^{(q)}$ and $\phi_{\lambda,k}^{(j)}$ are not equal to zero, i.e., both $m_\lambda^{(j)}$ and $m_\gamma^{(q)}$ are not nodes of the kth mode shape.

Appendix B

For an infinitely long AMM consisting of intact mass-in-mass units described in Fig. 1, the governing equations of its *j*th unit can expressed

$$\begin{bmatrix} m_{1} & 0 \\ 0 & m_{2} \end{bmatrix} \begin{Bmatrix} \ddot{u}_{1}^{(j)} \\ \ddot{u}_{2}^{(j)} \end{Bmatrix} + \begin{bmatrix} 2k_{1} + k_{2} & -k_{2} \\ -k_{2} & k_{2} \end{bmatrix} \times \begin{Bmatrix} u_{1}^{(j)} \\ u_{2}^{(j)} \end{Bmatrix} + \begin{bmatrix} -k_{1} & -k_{1} \\ 0 & 0 \end{bmatrix} \begin{Bmatrix} u_{1}^{(j-1)} \\ u_{1}^{(j+1)} \end{Bmatrix} = \begin{Bmatrix} 0 \\ 0 \end{Bmatrix}.$$
(B.1)

A harmonic wave solution to Eq. (B.1) can be expressed by

$$\begin{cases}
 u_1^{(j)} = u_{1,+x}^{(j)} + u_{1,-x}^{(j)} \\
 u_2^{(j)} = u_{2,+x}^{(j)} + u_{2,-x}^{(j)}
\end{cases} ,$$
(B.2)

where $u_{\nu_{+}\nu_{+}}^{(j)}$ and $u_{\nu_{-}\nu_{-}}^{(j)}$ are propagating components of the solution that advance in the +x and -x directions, respectively. Denote the position of the jth unit by x, for the (j + h)th unit, the propagating components can be expressed by

$$u_{\gamma,+x}^{(j+h)} = B_{\gamma,+x} e^{j(\omega t - qx)} e^{-hqL}$$
 (B.3)

$$u_{\nu,-x}^{(j+h)} = B_{\nu,-x} e^{j(\omega t + qx)} e^{hqL},$$
 (B.4)

where $B_{\gamma,+x}$ and $B_{\gamma,-x}$ are the complex wave amplitudes, j = $\sqrt{-1}$, and qL is the dimensionless wave number. Based on Eq. (B.3), $u_{\nu,+\nu}^{(j)}$ is expressed by

$$u_{1,+x}^{(j)} = B_{1,+x} e^{i(\omega t - qx)}$$
 (B.5)

$$u_{2 + x}^{(j)} = B_{2, +x} e^{j(\omega t - qx)}$$
 (B.6)

For the (j-1)th and (j+1)th units, one has

$$u_{1 + x}^{(j-1)} = B_{1, +x} e^{j(\omega t - qx)} e^{qL} = u_{1 + x}^{(j)} e^{qL}$$
(B.7)

$$u_{1,+x}^{(j+1)} = B_{1,+x} e^{j(\omega t - qx)} e^{-qL} = u_{1,+x}^{(j)} e^{-qL} ,$$
 (B.8)

respectively

When the harmonic solution contains only propagating components that advance in the +x direction, one has

$$u_1^{(j)} = u_{1+1}^{(j)} \tag{B.9}$$

and

$$u_2^{(j)} = u_{2,+x}^{(j)}$$
 (B.10)

Substituting Eqs. (B.5) through (B.10) into Eq. (B.1) and rearranging the resulting equations yield

$$\begin{bmatrix} -\omega^{2} m_{1} + 2k_{1} - k_{1} \left(e^{qL} + e^{-qL} \right) + k_{2} & -k_{2} \\ -k_{2} & -\omega^{2} m_{2} + k_{2} \end{bmatrix} \times \begin{cases} B_{1,+x} \\ B_{2,+x} \end{cases} e^{j(\omega t - qx)} = \begin{cases} 0 \\ 0 \end{cases}.$$
(B.11)

Applying

$$\cosh(qL) = \frac{e^{qL} + e^{-qL}}{2} \tag{B.12}$$

to Eq. (B.11) yields

$$\begin{bmatrix} -\omega^{2} m_{1} + 2k_{1} (1 - \cosh(qL)) + k_{2} & -k_{2} \\ -k_{2} & -\omega^{2} m_{2} + k_{2} \end{bmatrix} \times \begin{Bmatrix} B_{1,+x} \\ B_{2,+x} \end{Bmatrix} = \begin{Bmatrix} 0 \\ 0 \end{Bmatrix}.$$
 (B.13)

A linear equation set similar to Eq. (B.13) can be obtained when

$$u_1^{(j)} = u_{1-x}^{(j)} \tag{B.14}$$

and

$$u_2^{(j)} = u_{2-x}^{(j)},$$
 (B.15)

which can be expressed by

$$\begin{bmatrix} -\omega^{2}m_{1} + 2k_{1} (1 - \cosh(qL)) + k_{2} & -k_{2} \\ -k_{2} & -\omega^{2}m_{2} + k_{2} \end{bmatrix} \times \begin{Bmatrix} B_{1,-x} \\ B_{2,-x} \end{Bmatrix} = \begin{Bmatrix} 0 \\ 0 \end{Bmatrix}.$$
 (B.16)

$$\det \left(\begin{bmatrix} -\omega^2 m_1 + 2k_1 (1 - \cosh(qL)) + k_2 & -k_2 \\ -k_2 & -\omega^2 m_2 + k_2 \end{bmatrix} \right) = 0 \quad (B.17)$$

both Eqs. (B.13) and (B.16) have non-trivial solutions, and the dispersion equation associated with the AMM can be obtained from Eq. (B.17), which is expressed by

$$m_1 m_2 \omega^4 - \left(\left(m_1 + m_2 \right) k_2 + 2 m_2 k_1 \left(1 - \cosh \left(qL \right) \right) \right) \omega^2 + 2 k_1 k_2 \left(1 - \cosh \left(qL \right) \right) = 0$$
(B.18)

and it can lead to

$$\cosh(qL) = 1 + \frac{m_1 m_2 \omega^4 - (m_1 + m_2) k_2 \omega^2}{2k_1 (k_2 - m_2 \omega^2)}.$$
 (B.19)

$$qL = \alpha + j\beta \tag{B.20}$$

denote the complex dimensionless wave number, where α and β are

referred to as the attenuation constant and phase constant, respectively. For both $u_{\gamma,+x}^{(j+h)}$ in Eq. (B.3) and $u_{\gamma,-x}^{(j+h)}$ in Eq. (B.4) that propagate to the next units in their respective directions, i.e., $u_{\gamma,+x}^{(j+L)}$ and $u_{\gamma,-x}^{(j-L)}$, respectively, the complex term

$$e^{-hqL} = e^{-h\alpha}e^{-jh\beta} \tag{B.21}$$

exists. When $\alpha=0$, the magnitudes of $u_{\gamma,+x}^{(j+L)}$ and $u_{\gamma,-x}^{(j-L)}$ remain the same as h varies; when $\alpha > 0$, they exponentially decay as the waves propagate in their respective directions.

A non-trivial solution to Eq. (B.13) can be expressed by

$$\begin{cases}
B_{1,+x} = -\omega^2 m_2 + k_2 \\
B_{2,-x} = k_2
\end{cases}$$
(B.22)

The ratio between $B_{1,+x}$ and $B_{2,+x}$ can be expressed by

$$\frac{B_{1,+x}}{B_{2,+x}} = 1 - \frac{\omega^2}{\omega_0^2} = 1 - \bar{\omega}^2.$$
 (B.23)

When $\omega < \omega_0$, i.e., $\bar{\omega} < 1$, the values of $B_{1,+x}$ and $B_{2,+x}$ in Eq. (B.22) are of the same sign, and the associated solutions are considered to be in the acoustical mode. When $\omega > \omega_0$, i.e., $\bar{\omega} > 1$, the values of $B_{1,+x}$ and $B_{2,+x}$ in Eq. (B.22) are of the different signs, and the associated solutions are considered to be in the optical mode. The same observations apply to a non-trivial solution to Eq. (B.16), which can be

$$\begin{cases}
B_{1,-x} = -\omega^2 m_2 + k_2 \\
B_{2,-x} = k_2
\end{cases}$$
(B.24)

$$\frac{B_{1,-x}}{B_{2,-x}} = 1 - \frac{\omega^2}{\omega_0^2} = 1 - \bar{\omega}^2.$$
 (B.25)

References

- [1] Liu Z, Zhang X, Mao Y, Zhu Y, Yang Z, Chan CT, et al. Locally resonant sonic materials. Science 2000;289(5485):1734-6.
- [2] Li J, Chan CT. Double-negative acoustic metamaterial. Phys Rev E 2004;70(5):055602.

- [3] Peng H, Pai PF, Deng H. Acoustic multi-stopband metamaterial plates design for broadband elastic wave absorption and vibration suppression. Int J Mech Sci 2015;103:104-14
- [4] Cummer SA, Christensen J, Alù A. Controlling sound with acoustic metamaterials. Nat Rev Mater 2016;1(3):1–13.
- [5] Ma G, Sheng P. Acoustic metamaterials: From local resonances to broad horizons. Sci Adv 2016;2(2):e1501595.
- [6] Hussein MI, Leamy MJ, Ruzzene M. Dynamics of phononic materials and structures: Historical origins, recent progress, and future outlook. Appl Mech Rev 2014;66(4)
- [7] Lim C. From photonic crystals to seismic metamaterials: A review via phononic crystals and acoustic metamaterials. Arch Comput Methods Eng 2022;29(2):1137–98.
- [8] Zhu R, Liu X, Hu G, Sun C, Huang G. A chiral elastic metamaterial beam for broadband vibration suppression. J Sound Vib 2014;333(10):2759–73.
- [9] Hu G, Austin AC, Sorokin V, Tang L. Metamaterial beam with graded local resonators for broadband vibration suppression. Mech Syst Signal Process 2021;146:106982.
- [10] Man X, Xia B, Luo Z, Liu J, Li K, Nie Y. Engineering three-dimensional labyrinthine fractal acoustic metamaterials with low-frequency multi-band sound suppression. J Acoust Soc Am 2021;149(1):308–19.
- [11] Fang X, Sheng P, Wen J, Chen W, Cheng L. A nonlinear metamaterial plate for suppressing vibration and sound radiation. Int J Mech Sci 2022;228:107473.
- [12] Elford DP, Chalmers L, Kusmartsev FV, Swallowe GM. Matryoshka locally resonant sonic crystal. J Acoust Soc Am 2011;130(5):2746-55.
- [13] Meng H, Wen J, Zhao H, Wen X. Optimization of locally resonant acoustic metamaterials on underwater sound absorption characteristics. J Sound Vib 2012;331(20):4406–16.
- [14] Matsuki T, Yamada T, Izui K, Nishiwaki S. Topology optimization for locally resonant sonic materials. Appl Phys Lett 2014;104(19):191905.
- [15] Gulia P, Gupta A. Sound attenuation in triple panel using locally resonant sonic crystal and porous material. Appl Acoust 2019;156:113–9.
- [16] Liu Z, Chan CT, Sheng P. Analytic model of phononic crystals with local resonances. Phys Rev B 2005;71(1):014103.
- [17] Milton GW, Willis JR. On modifications of Newton's second law and linear continuum elastodynamics. Proc R Soc Lond Ser A Math Phys Eng Sci 2007;463(2079):855–80.
- [18] Huang H, Sun C, Huang G. On the negative effective mass density in acoustic metamaterials. Internat J Engrg Sci 2009;47(4):610–7.
- [19] Huang G, Sun C. Band gaps in a multiresonator acoustic metamaterial. J Vib Acoust 2010;132(3).
- [20] Oudich M, Senesi M, Assouar MB, Ruzenne M, Sun JH, Vincent B, et al. Experimental evidence of locally resonant sonic band gap in two-dimensional phononic stubbed plates. Phys Rev B 2011;84(16):165136.
- [21] Baravelli E, Ruzzene M. Internally resonating lattices for bandgap generation and low-frequency vibration control. J Sound Vib 2013;332(25):6562–79.
- [22] Nouh M, Aldraihem O, Baz A. Wave propagation in metamaterial plates with periodic local resonances. J Sound Vib 2015;341:53–73.
- [23] Matlack KH, Bauhofer A, Krödel S, Palermo A, Daraio C. Composite 3D-printed metastructures for low-frequency and broadband vibration absorption. Proc Natl Acad Sci 2016;113(30):8386–90.
- [24] Farrar CR, Worden K. An introduction to structural health monitoring. Phil Trans R Soc A 2007;365(1851):303–15.
- [25] Avci O, Abdeljaber O, Kiranyaz S, Hussein M, Gabbouj M, Inman DJ. A review of vibration-based damage detection in civil structures: From traditional methods to machine learning and deep learning applications. Mech Syst Signal Process 2021;147:107077.
- [26] Kaewniam P, Cao M, Alkayem NF, Li D, Manoach E. Recent advances in damage detection of wind turbine blades: A state-of-the-art review. Renew Sustain Energy Rev 2022;167:112723.
- [27] Wu X, Su Y, Shi J. Perspective of additive manufacturing for metamaterials development. Smart Mater Struct 2019;28(9):093001.
- [28] Askari M, Hutchins DA, Thomas PJ, Astolfi L, Watson RL, Abdi M, et al. Additive manufacturing of metamaterials: A review. Addit Manuf 2020;36:101562.
- [29] Montgomery SM, Kuang X, Armstrong CD, Qi HJ. Recent advances in additive manufacturing of active mechanical metamaterials. Curr Opin Solid State Mater Sci 2020:24(5):100869.
- [30] Hirsch M, Catchpole-Smith S, Patel R, Marrow P, Li W, Tuck C, et al. Meso-scale defect evaluation of selective laser melting using spatially resolved acoustic spectroscopy. Proc R Soc Lond Ser A Math Phys Eng Sci 2017;473(2205):20170194.
- [31] Sola A, Nouri A. Microstructural porosity in additive manufacturing: The formation and detection of pores in metal parts fabricated by powder bed fusion. J Adv Manuf Process 2019;1(3):e10021.
- [32] Lee JH, Lee CM, Kim DH. Repair of damaged parts using wire arc additive manufacturing in machine tools. J Mater Res Tech 2022;16:13–24.
- [33] Zhai Y, Galarraga H, Lados DA. Microstructure, static properties, and fatigue crack growth mechanisms in Ti-6Al-4V fabricated by additive manufacturing: LENS and EBM. Eng Fail Anal 2016;69:3–14.

- [34] Gordon J, Haden C, Nied H, Vinci R, Harlow D. Fatigue crack growth anisotropy, texture and residual stress in austenitic steel made by wire and arc additive manufacturing. Mater Sci Eng A 2018;724:431–8.
- [35] Verstrynge E, Lacidogna G, Accornero F, Tomor A. A review on acoustic emission monitoring for damage detection in masonry structures. Constr Build Mater 2021;268:121089.
- [36] Arora V, Wijnant YH, de Boer A. Acoustic-based damage detection method. Appl Acoust 2014;80:23–7.
- [37] Mitra M, Gopalakrishnan S. Guided wave based structural health monitoring: A review. Smart Mater Struct 2016;25(5):053001.
- [38] Guan R, Lu Y, Duan W, Wang X. Guided waves for damage identification in pipeline structures: A review. Struct Control Health Monit 2017;24(11):e2007.
- [39] Saeedifar M, Zarouchas D. Damage characterization of laminated composites using acoustic emission: A review. Composites B 2020;195:108039.
- [40] Rahman Z, Ohba H, Yoshioka T, Yamamoto T. Incipient damage detection and its propagation monitoring of rolling contact fatigue by acoustic emission. Tribol Int 2009;42(6):807–15.
- [41] Behnia A, Chai HK, Ranjbar N, Jumaat MZ. Damage detection of SFRC concrete beams subjected to pure torsion by integrating acoustic emission and Weibull damage function. Struct Control Health Monit 2016;23(1):51–68.
- [42] Xu Y, Kim J. Baseline-free structural damage identification for beam-like structures using curvature waveforms of propagating flexural waves. Sensors 2021;21(7):2453.
- [43] Zhou W, Xu Y, Kim J. Baseline-free structural damage identification for plate-like structures based on two-dimensional curvature propagating flexural waves. J Sound Vib 2022;536:117098.
- [44] Zhou W, Xu Y. Damage identification for beam-like structures based on proper orthogonal modes of guided wavefields. Mech Syst Signal Process 2023;189:110052.
- [45] Gómez Muñoz CQ, García Márquez FP, Hernández Crespo B, Makaya K. Structural health monitoring for delamination detection and location in wind turbine blades employing guided waves. Wind Energy 2019;22(5):698–711.
- [46] Hervin F, Maio L, Fromme P. Guided wave scattering at a delamination in a quasi-isotropic composite laminate: Experiment and simulation. Compos Struct 2021:275:114406.
- [47] Yu L, Tian Z, Li X, Zhu R, Huang G. Core–skin debonding detection in honeycomb sandwich structures through guided wave wavefield analysis. J Intell Mater Syst Struct 2019;30(9):1306–17.
- [48] Zima B, Kędra R. Reference-free determination of debonding length in reinforced concrete beams using guided wave propagation. Constr Build Mater 2019;207:291–303.
- [49] Shi Z, Law S, Zhang L. Structural damage detection from modal strain energy change. J Eng Mech 2000;126(12):1216–23.
- [50] Guan H, Karbhari VM. Improved damage detection method based on element modal strain damage index using sparse measurement. J Sound Vib 2008;309(3–5):465–94.
- [51] Doebling SW, Farrar CR, Prime MB, Shevitz DW. Damage identification and health monitoring of structural and mechanical systems from changes in their vibration characteristics: a literature review. Los Alamos, NM (United States): Los Alamos National Lab.(LANL); 1996.
- [52] Turner A, Graver TW. Structural monitoring of wind turbine blades using fiber optic bragg grating strain sensors. In: Experimental mechanics on emerging energy systems and materials, volume 5: Proceedings of the 2010 annual conference on experimental and applied mechanics. Springer; 2011, p. 149–54.
- [53] Bastianini F, Matta F, Rizzo A, Galati N, Nanni A. Overview of recent bridge monitoring applications using distributed brillouin fiber optic sensors. J Nondestruct Test 2007;12(9):269–76.
- [54] Zhu W, He K. Detection of damage in space frame structures with L-shaped beams and bolted joints using changes in natural frequencies. J Vib Acoust 2013;135(5).
- [55] Qiao W, Ma B, Liu Q, Wu X, Li G. Computer vision-based bridge damage detection using deep convolutional networks with expectation maximum attention module. Sensors 2021;21(3):824.
- [56] van Ruitenbeek R, Bhulai S. Convolutional neural networks for vehicle damage detection. Mach Learn Appl 2022;9:100332.
- [57] Shihavuddin A, Chen X, Fedorov V, Nymark Christensen A, Andre Bro-gaard Riis N, Branner K, et al. Wind turbine surface damage detection by deep learning aided drone inspection analysis. Energies 2019;12(4):676.
- [58] Simoen E, De Roeck G, Lombaert G. Dealing with uncertainty in model updating for damage assessment: A review. Mech Syst Signal Process 2015;56:123–49.
- [59] Takano N, Takizawa H, Wen P, Odaka K, Matsunaga S, Abe S. Stochastic prediction of apparent compressive stiffness of selective laser sintered lattice structure with geometrical imperfection and uncertainty in material property. Int J Mech Sci 2017:134:347–56.
- [60] Balokas G, Czichon S, Rolfes R. Neural network assisted multiscale analysis for the elastic properties prediction of 3D braided composites under uncertainty. Compos Struct 2018;183:550–62.
- [61] An H, Youn BD, Kim HS. Reliability-based design optimization of laminated composite structures under delamination and material property uncertainties. Int J Mech Sci 2021;205:106561.

- [62] Rupal BS, Anwer N, Secanell M, Qureshi AJ. Geometric tolerance and manufacturing assemblability estimation of metal additive manufacturing (AM) processes. Mater Des 2020;194:108842.
- [63] Minetola P, Calignano F, Galati M. Comparing geometric tolerance capabilities of additive manufacturing systems for polymers. Addit Manuf 2020;32:101103.
- [64] Alkayem NF, Cao M, Zhang Y, Bayat M, Su Z. Structural damage detection using finite element model updating with evolutionary algorithms: a survey. Neural Comput Appl 2018;30:389–411.
- [65] Gomes H, Silva N. Some comparisons for damage detection on structures using genetic algorithms and modal sensitivity method. Appl Math Model 2008;32(11):2216–32.
- [66] Lin Yz, Nie Zh, Ma Hw. Structural damage detection with automatic feature-extraction through deep learning. Comput-Aided Civ Infrastruct Eng 2017;32(12):1025–46.
- [67] Sha G, Radzieński M, Cao M, Ostachowicz W. A novel method for single and multiple damage detection in beams using relative natural frequency changes. Mech Syst Signal Process 2019;132:335–52.

- [68] Allemang RJ. The modal assurance criterion-twenty years of use and abuse. Sound Vib 2003;37(8):14-23.
- [69] Al Ba'ba'a H, Nouh M, Singh T. Formation of local resonance band gaps in finite acoustic metamaterials: A closed-form transfer function model. J Sound Vib 2017;410:429–46.
- [70] Ghosh G, Ray-Chaudhuri S. Location sensitivity of fundamental and higher mode shapes in localization of damage within a building. J Sound Vib 2016;365:244–59.
- [71] Bartilson DT, Jang J, Smyth AW. Symmetry properties of natural frequency and mode shape sensitivities in symmetric structures. Mech Syst Signal Process 2020:143:106797.
- [72] Mottershead JE, Ram YM. Inverse eigenvalue problems in vibration absorption: passive modification and active control. Mech Syst Signal Process 2006;20(1):5–44.
- [73] Mottershead J. On the zeros of structural frequency response functions and their sensitivities. Mech Syst Signal Process 1998;12(5):591–7.
- [74] Javh J, Slavič J, Boltežar M. High frequency modal identification on noisy high-speed camera data. Mech Syst Signal Process 2018;98:344–51.